Applied Magnetic Resonance (2022) 53:745–761
https://doi.org/10.1007/s00723-021-01388-1

Applied
Magnetic Resonance

ORIGINAL PAPER

Short-Time Dynamics of Radical-Ion Pairs Produced by Photoinduced Electron Transfer in Solution: The Magnetic Field Effect

Serguei V. Feskov[1] · **Anatoly I. Ivanov**[1]

Received: 8 May 2021 / Revised: 23 June 2021 / Accepted: 7 July 2021 /
Published online: 26 July 2021

Abstract

Kinetics of radical-ion pairs (RIPs) formed by photoinduced electron transfer in solution, as well as triplet and singlet products of their recombination, are studied within a general theory of spin-selective charge transfer assisted by diffusion of reactants in solution. The RIPs are assumed to be created in the singlet state, and their coherent singlet–triplet evolution is described in terms of isotropic hyperfine interaction (HFI) and Δg mechanisms. A set of quantum-classical model equations is solved numerically using the time propagator splitting technique. Numerical simulations are carried out on a prototype photochemical reaction involving bimolecular electron transfer between 9,10-dimethylanthracene (DMeA) and phthalonitrile (PN) in acetonitrile (ACN) solution. Time-dependent populations of all electronic and spin states, as well as spatial distributions of reactants in the course of forward and backward charge transfer are calculated and analysed. Particularly, spatial profiles of charge recombination (CR) in singlet and triplet RIPs are shown to differ significantly, with a significant part of the singlet RIPs undergoing distant (non-contact) recombination. The effect of a strong (saturating) magnetic field on the triplet CR product yield in these reactions is studied. For the HFI-induced coherent spin transitions, the time-dependent magnetic field effect is shown to decrease with time. A phenomenon of suppressing the triplet CR product yield in RIPs with the HFI- and Δg-induced coherent spin transitions in moderate magnetic fields is investigated and its physical origins are discussed.

✉ Anatoly I. Ivanov
anatoly.ivanov@volsu.ru

[1] Volgograd State University, University Avenue 100, Volgograd 400062, Russia

1 Introduction

Discovery of magnetic and spin effects in radical reactions and clarification their mechanisms [1] has triggered widespread research of photoinduced electron transfer (ET) processes, where radical ions are typically formed. It has been shown that a presence in solution of molecules with the electron-accepting and electron-donating capabilities often leads to quenching of either the excited donor or the excited acceptor emission. This phenomenon was interpreted in terms of intermolecular ET from the donor D molecule to the acceptor molecule A, leading to formation of a radical-ion pair according to one of the following schemes: $D^* + A \rightarrow {}^2D^+ + {}^2A^-$ or $D + A^* \rightarrow {}^2D^+ + {}^2A^-$ [2–5]. In these schemes, one of the reactants acts as a photosensitizer and a fluorophore, while another acts as a quencher, so in what follows we denote these molecules as F and Q. Since the total spin of the pair during the elementary ET step is conserved, the excited singlet (precursor) pair $^1F^*+Q$ creates a RIP in the singlet state; however, this pair can recombine some time later due to singlet–triplet transitions and produce neutral products with a fluorophore in the triplet excited state, $^3F^*+Q$ [6–15]. This clearly demonstrates the mechanism of the $^1F^*$ fluorescence quenching and the $^3F^*$ state formation in these processes, which is due to spin conversion at the stage of geminate radical-ion pairs (see Fig. 1) [6, 7, 12]. This mechanism was elegantly established in photoinduced ET reactions involving pyrene and dimethylaniline [12], where hyperfine interactions (HFI) was shown to produce spin conversion in RIPs. The probability of recombination of uncharged radicals in the zero magnetic field accounting for the singlet–triplet mixing induced by isotropic HFI was first obtained in Ref. [16]. Later, the HFI-mechanism was used to explain the influence of solvent viscosity on the yield of the neutral triplet products [17, 18]. This mechanism was also successfully applied to a quantitative description of the magnetic field effect (MFE) in the fluorophore and exciplex fluorescence, as well as the MFE dependence on solvent viscosity and polarity [19, 20].

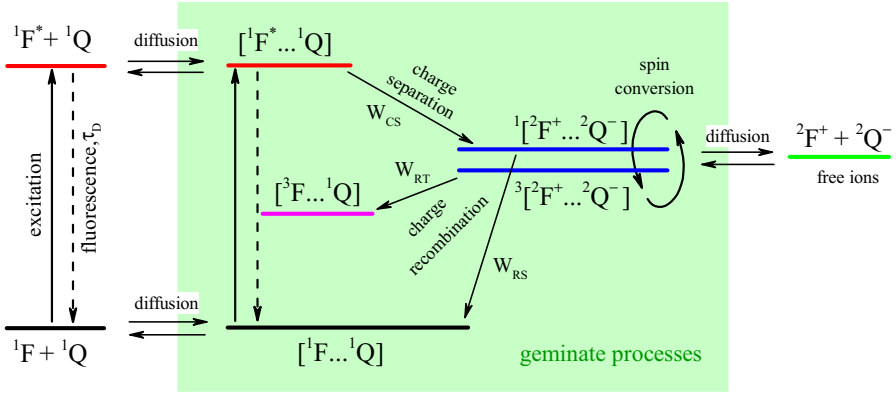

Fig. 1 Overall scheme of fluorescence quenching by electron transfer in solution. F and Q are the fluorophore and quencher molecules. Geminate processes include radiative decay of F^* with a characteristic time scale τ_D, photoinduced forward ET from F^* to Q (charge separation), spin transitions in radical-ion pairs, and spin-selective back ET from Q to F^+ (charge recombination)

In non-viscous solvents, geminate processes typically occur within the 0–50 ns time window. High-resolution experimental studies of the radical-ion and triplet neutral states kinetics in this time window have become available only recently using optical spectroscopy techniques [21]. The sub-nanosecond time resolution was achieved (an instrument response function of 350 ps (fwhm)) [21]. Although multifrequency electron paramagnetic resonance spectroscopy has many advantages over optical spectroscopy, it cannot provide such temporal resolution [22]. Numerical simulations have also demonstrated that time-dependent concentrations of the ion pairs and triplet neutral ET products in these processes can be well reproduced using the HFI mechanism both in a zero magnetic field and in saturated magnetic field limits in polar solvents [21]. It has also been shown in simulations that satisfactory description of the RIP formation in zero magnetic field effects can be achieved only within a Hamiltonian (coherent) model of singlet–triplet transitions [21]. On the other hand, describing spin conversion in terms of rates strongly overestimates the magnetic field effect on the triplet product yield.

Naturally, the HFI-mechanism of spin conversion is not the only possible reason of singlet–triplet mixing in RIPs. Paramagnetic relaxation of electron spins due to their interaction with solvent molecules and the Δg-mechanism in magnetic fields can also be operative [6, 11, 12, 23]. However, in organic radical-ions, the paramagnetic relaxation is quite slow and usually cannot compete with the HFI-mechanism [23].

Although the triplet products of charge recombination in RIPs can be formed by both geminate and non-geminate recombination, the concentration of radical ions in typical experiments is so low, that bulk recombination proceeds only on a microsecond time scale, while geminate recombination generally takes place on a nanosecond time scale. In this study, we, therefore, restrict our consideration to the geminate phase of the reaction and neglect charge recombination processes involving ions from different RIPs.

In Ref. [21], the kinetics of radical ions and triplet neutral products in zero and strong (saturated) magnetic fields were reported. In this contribution, we investigate the magnetic field effect on the triplet product yield when two mechanisms, HFI and Δg, are operative. We show that for typical values of the effective HFI constant and large $\Delta g \approx 10^{-2}$, which is still achievable for organic radical ions, the competition between these two mechanisms can completely suppress charge recombination to form neutral triplet products.

2 Theory

The model used in this paper is similar to that described earlier in Ref. [21]. As suggested by the scheme in Fig. 1, the F^* fluorescence quenching in solution is a multistage reaction assisted by diffusion of the reactant molecules, and involves forward and backward electron transfer in the course of their diffusive encounters. Kinetics of these bimolecular processes are well described within the encounter theory of fluorescence quenching and RIP formation/decay [5, 13, 15, 17, 24–29]. The theory

operates with the survival probability $N(t)$ of the excited fluorophore, which obeys the equation [26]:

$$\dot{N}(t) = -ck_{\mathrm{CS}}(t)N(t) - N(t)/\tau_{\mathrm{F}}, \quad k_{\mathrm{I}}(t) = \int W_{\mathrm{CS}}(r)n(r,t)\,d^3r, \quad N(0) = 1, \quad (1)$$

were $k_{\mathrm{CS}}(t)$ is the time-dependent charge separation (CS) rate constant, and τ_{F} is the lifetime of fluorophore F^* in the first excited state S_1 in the absence of quenchers. The quencher concentration c is assumed to be large enough so that its evolution in time can be neglected. The distribution function $n(r, t)$ of the $\mathrm{F}^*\mathrm{Q}$ pairs over the distances r between the molecules is given by the equation:

$$\frac{\partial n(r,t)}{\partial t} = -W_{\mathrm{CS}}(r)n(r,t) + \hat{L}n(r,t), \quad (2)$$

where

$$\hat{L} = \frac{D}{r^2}\frac{\partial}{\partial r}r^2\frac{\partial}{\partial r} \quad (3)$$

is the operator of encounter diffusion of neutral reactants with D being the diffusion coefficient. In a typical experiment, the F^* and Q molecules are uniformly distributed over the entire volume before excitation at $t = 0$, so that the initial condition for Eq. (2) is usually written as $n(r, 0) = 1$.

Spin evolution of RIPs proceeding after charge separation is described in terms of the r-dependent spin density matrix $\hat{m}(r, t)$ and is governed by the spin Hamiltonian:

$$\hat{H} = \hat{H}_{\mathrm{el}} + \hat{H}_{\mathrm{hfi}}, \quad (4)$$

where

$$\hat{H}_{\mathrm{el}} = \omega_{\mathrm{F}}\hat{S}_{\mathrm{F}z} + \omega_{\mathrm{Q}}\hat{S}_{\mathrm{Q}z} + J(r)\left(\frac{1}{2} + 2\hat{\mathbf{S}}_{\mathrm{F}} \cdot \hat{\mathbf{S}}_{\mathrm{Q}}, \right). \quad (5)$$

The first two summands here indicate interaction of magnetic moments with an external magnetic field, and the third one describes the distance-dependent splitting $J(r)$ between the singlet and triplet states in RIP. S_{F} and S_{Q} are the 1/2 spins of the fluorophore and quencher, $\omega_{\mathrm{F}} = g_{\mathrm{F}}\mu_e B$ and $\omega_{\mathrm{Q}} = g_{\mathrm{Q}}\mu_e B$ are the Larmor frequencies of F^+ and Q^- radical ions in magnetic field B, g_{F} and g_{Q} are the electronic g factors, and μ_e is the Bohr's magneton. The $\hat{H}_{\mathrm{hfi}}$ operator in Eq. (4) represents isotropic HFI between the electronic spin $S_{\mathrm{F}} = 1/2$ and the effective nuclear spin $I = 1/2$:

$$\hat{H}_{\mathrm{hfi}} = A\hat{\mathbf{I}} \cdot \hat{\mathbf{S}}_{\mathrm{F}} \quad (6)$$

with A being the HFI coupling constant.

The possibility to model the interactions between the electronic spin and a number of nuclear spins by the interaction with a single nuclear spin with an effective HFI constant was discussed earlier in Ref. [16]. In the case of the 9,10-dimethylanthracene and phthalonitrile (DMeA/PN) pair, the HFI constants for all radical ions have been measured [30, 31]. Here, we consider only

the interaction with the fluorophore spin, since the effective HFI constant for ^{2}DMeA$^{\cdot+}$ is more than three times larger than that for ^{2}PN$^{\cdot-}$.

Interaction of electron and nuclear spins is described in terms of effective HFI constant, which is calculated as [16]

$$A = 2\sqrt{\frac{1}{3}\sum a_k^2 I_k(I_k+1)}, \tag{7}$$

where a_k are the HFI constants of the radical ions, and I_k are nuclear spins of both radical ions. The model with an effective spin was shown to be applicable for modeling short-time spin dynamics. For organic radical ions, typical values of the effective HFI constant is $A = 10^7 - 10^9$ s^{-1}.

Due to the conservation of the z-projection of the total spin:

$$\hat{\Sigma}_z = \hat{S}_{Fz} + \hat{S}_{Qz} + \hat{I}_z,$$

the spin ensemble decomposes into two equivalent non-interacting subensembles with a certain projection of the total spin $\hat{\Sigma}_z$ [32]. Each subensemble includes only three states:

$$|S,\alpha\rangle = \frac{1}{\sqrt{2}}(\alpha_e\beta_e - \beta_e\alpha_e)\alpha_N, |T_0,\alpha\rangle = \frac{1}{\sqrt{2}}(\alpha_e\beta_e + \beta_e\alpha_e)\alpha_N, |T_+,\beta\rangle = \alpha_e\alpha_e\beta_N. \tag{8}$$

The $\hat{m}(r,t)$ operator obeys the equation [26, 33–35]:

$$\frac{\partial\hat{m}(r,t)}{\partial t} = \hat{\hat{L}}\hat{m}(r,t) - i[\hat{H},\hat{m}(r,t)] - \frac{1}{2}\{\hat{W}_{\mathrm{R}}(r),\hat{m}(r,t)\} + \hat{f}(r,t), \tag{9}$$

where $\hat{H}$ is given by Eq. (4), $\hat{W}_{\mathrm{R}}$ is the reaction operator, and [...] and {...} stand for the commutator and anticommutator, respectively. The operator of spatial diffusion:

$$\hat{\hat{L}} = \frac{D}{r^2}\frac{\partial}{\partial r}r^2\, e^{-V/k_BT}\frac{\partial}{\partial r}e^{V/k_BT} \tag{10}$$

accounts for the Coulomb interaction between the ions $V(r) = -\frac{e^2}{\varepsilon(r)r}$ and spatial dispersion of the dielectric constant in the form [36]:

$$\varepsilon(r) = \frac{\varepsilon_0}{1 + \left(\frac{\varepsilon_0}{\varepsilon_\infty - 1}\right)\gamma\exp(-r/\Lambda)}, \tag{11}$$

where $\gamma = 2(\Lambda^2/\sigma^2)(\mathrm{ch}(\sigma/\Lambda) - 1)$ [36], ε_∞ and ε_0 are the optical and static dielectric constants, σ is the contact radius. In simulations, the correlation length of solvent polarization fluctuations was set to $\Lambda = 1.6$ Å, which roughly corresponds to the size of the acetonitrile molecule.

The term $\hat{f}(r,t)$ is given by [26]

$$\hat{f}(r,t) = W_{\mathrm{CS}}(r)n(r,t)N(t)\hat{P}_{\mathrm{S}}/\mathrm{Tr}\{\hat{P}_{\mathrm{S}}\}. \tag{12}$$

The auxiliary functions $n(r, t)$ and $\hat{m}(r, t)$ obey reflective boundary conditions at the contact radius $r = \sigma$:

$$\hat{J}_n n\Big|_{r=\sigma} = 4\pi r^2 D\,\frac{\partial n}{\partial r}\Big|_{r=\sigma} = 0, \quad \hat{J}_m \hat{m}(r,t)\Big|_{r=\sigma} = 4\pi r^2 D e^{-V/k_B T}\frac{\partial}{\partial r}e^{V/k_B T}\hat{m}\Big|_{r=\sigma} = 0. \tag{13}$$

where $\hat{J}_n$ and $\hat{J}_m$ are the diffusive flux operators for the neutral reactants and RIPs, correspondingly. The initial condition for Eq. (9) is $\hat{m}(r, 0) = 0$.

The reaction operator $\hat{W}_{\mathrm{R}}(r)$ quantifies the recombination rates of the RIPs to both the ground singlet and the triplet excited state of DMeA with the rate $W_{\mathrm{RS}}(r)$ and $W_{\mathrm{RT}}(r)$, respectively, so that

$$\hat{W}_{\mathrm{R}}(r) = W_{\mathrm{RS}}(r)\hat{P}_{\mathrm{S}} + W_{\mathrm{RT}}(r)\hat{P}_{\mathrm{T}}, \tag{14}$$

where $W_{\mathrm{RS}}(r)$ and $W_{\mathrm{RT}}(r)$ are the recombination rates of the RIPs to the ground singlet S_0 and the triplet T_1 excited state of the fluorophore, respectively, $\hat{P}_{\mathrm{S}}$ and $\hat{P}_{\mathrm{T}}$ are the singlet and triplet projection operators. Time-dependent populations of the singlet and triplet CR products are then calculated as [26]

$$\begin{aligned} P_{\mathrm{S}}(t) &= \frac{c}{2}\int W_{\mathrm{RS}}(r)\mathrm{Tr}\{\hat{P}_{\mathrm{S}}, \hat{m}(r,t)\}\, d^3 r = \psi_{\mathrm{RIP}}\varphi_{\mathrm{S}}(t), \\ P_{\mathrm{T}}(t) &= \frac{c}{2}\int W_{\mathrm{RT}}(r)\mathrm{Tr}\{\hat{P}_{\mathrm{T}}, \hat{m}(r,t)\}\, d^3 r = \psi_{\mathrm{RIP}}\varphi_{\mathrm{T}}(t), \end{aligned} \tag{15}$$

where

$$\psi_{\mathrm{RIP}} = c\int d^3 r \int_0^\infty \mathrm{Tr}\hat{f}(r,t)\, dt \tag{16}$$

is the quantum yield of primary RIP, $\varphi_{\mathrm{S}}(t)$ and $\varphi_{\mathrm{T}}(t)$ are the probabilities of the singlet, CR0, and triplet, CR1, charge recombination of the RIP up to the time moment t. The probability of diffusive separation of the RIP into free ions is $\varphi_{\mathrm{sep}}(t) = 1 - \varphi_{\mathrm{S}}(t) - \varphi_{\mathrm{T}}(t)$, and the yield of free ions to the bulk is $\phi = \psi_{\mathrm{RIP}}\varphi_{\mathrm{sep}}$.

The charge separation and charge recombination rate constants are given by [37]

$$W_j(r) = V_j^2(r)\sqrt{\frac{\pi}{\lambda(r)k_{\mathrm{B}}T}}\sum_{n=0}^{\infty}\frac{S^n e^{-S}}{n!}\exp\left\{-\frac{[\Delta G_j + \lambda(r) + \Omega n]^2}{4\lambda(r)k_{\mathrm{B}}T}\right\}. \tag{17}$$

where the distance-dependent reorganization energy $\lambda(r)$ is

$$\lambda(r) = \lambda_i + \lambda_m\left(2 - \frac{\sigma}{r}\right), \tag{18}$$

λ_i and λ_m are associated with the reorganization of low-frequency intramolecular modes and the medium, respectively. The j index here runs the values $j = \mathrm{CS}$, RS, and RT, corresponding to charge separation and charge recombination into the

singlet and triplet states of neutral products, respectively. The coupling energies $V_j(r)$ of these electronic states are modelled as $V_j(r) = V_j(\sigma)\exp(-(r-\sigma)/L)$, where L is the electron tunnelling length, ΔG_j are the driving forces of the corresponding ET reactions, $S = \lambda_q/\hbar\Omega$ is the electron-vibration (Huang-Rhys) parameter [38], λ_q is the reorganization energy of the high-frequency intramolecular vibrational mode with the frequency Ω.

3 Simulation Results

In this section, we discuss the results of numerical simulations elucidating some important features of the multistage process in Fig. 1. Particularly, these results illustrate how coherent spin evolution produced by HFI and the Δg-interactions with an external magnetic field can manifest itself in the CR kinetics and CR product yields. Our analysis is based on numerical solution of Eqs. (1, 2, 3, 4, 5, 6, 7, 8, 9, 10, 11, 12, 13, 14, 15, 16, 17, 18) using the FLUT code [39]. Modular structure of the code allows configuring the CS/CR reaction model by setting the parameters of reactants mobility in a liquid and specifying the electronic/vibrational states involved in the reaction as well as intensities/types of transitions between them. The package is implemented as a set of C++ classes representing several basic concepts of the model, such as the diffusive space for the reactant pair, the distance-dependent CT coupling between the molecules, the electronic and vibrational de-excitation due to radiative and non-radiative transitions, and the Hamiltonian dynamics of the spin subsystem.

From computational point of view, the most expensive part of the algorithm is solving Eq. (9) for the density matrix $\hat{m}(r,t)$. This equation represents quantum-classical dynamics of RIPs including diffusive evolution along the r coordinate and coherent spin transitions. Our numerical method is based on calculation of the $\hat{m}(r,t)$ propagator using the Trotter splitting scheme for the elementary processes. Specifically, the radial diffusion of reactants is calculated within the Chebyshev time propagation algorithm obeying the detailed balance conditions [41]. The spin dynamics are simulated by splitting the Hamiltonian matrix $\hat{H}$ into several components, that allows one to evaluate the corresponding component propagators analytically. The matrix splitting method is justified for sufficiently small time steps Δt, which are less than time scales of all spin transitions in the system. In numerical experiments presented here, we used the time step $\Delta t = 0.25$ ps that provided the required precision and convergence of the results. The accuracy of computations was also controlled in the course of the experiment: particularly, simple normalization tests have shown the overall population for all electronic states in the system to deviate from unity by no more than 10^{-7} over the entire time interval of simulation.

Consider now a general scenario of the photoreaction pictured in Fig. 1, taking the 9,10-dimethylanthracene and phthalonitrile (DMeA/PN) pair as a prototype molecular system, where DMeA acts as a fluorophore and primary electron donor, and PN as a quencher and primary acceptor. We note that the layout of the first excited state of the fluorophore S_1 and the charge separated state *CSS* energy levels in this system (shown in Fig. 2) facilitates fast and efficient photoinduced

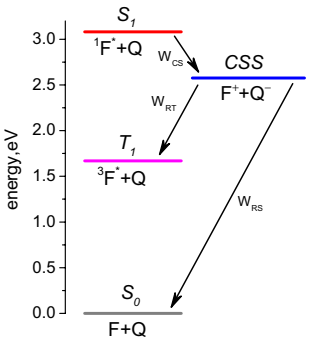

Fig. 2 Energy diagram of the photochemical processes with participation of 9,10-dimethylanthracene (DMeA, fluorophore F) and phthalonitrile (PN, quencher Q). S_1 and T_1 are the singlet and triplet excited states, S_0 is the ground state, and *CSS* is the charge-separated (ion-radical) state of the pair. The *CSS* energy level corresponds to the contact arrangement of radical-ions in acetonitrile ($\varepsilon = 36$) [40]

ET from F*'s to nearby Q's even at sufficiently small concentrations of quenchers. Indeed, the CS here is moderately exergonic with the driving force $\Delta G_{CS} = -0.5$ eV [40]. The absolute value of ΔG_{CS} is close to the solvent reorganization energy λ_m in many polar solvents (for example, in acetonitrile ACN it is estimated as ~ 0.75 eV), that provides low-barrier and fast electronic transition from S_1 to *CSS* and efficient quenching of the F* fluorescence. This conclusion is confirmed by simulation results shown in Fig. 3 (panel A), where the time-dependent populations of the S_1, *CSS*, and T_1 and S_0 states are shown at the stage of the CS reaction in the 0–0.8 ns time interval. The values of the model parameters used in these simulations are listed in Table 1.

Typical simulation show fast decay of the S_1 state during a few hundreds of ps immediately after excitation (red curve in Fig. 3A). This decay is much faster than radiative de-excitation of the excited fluorophore (the lifetime of the DMeA* fluorescence in ACN is known to be $\tau_D = 7.9$ ns) and clearly indicates strong quenching of F* by electron transfer. The S_1 decay in Fig. 3A is accompanied by simultaneous growth of the *CSS* population (blue curve) that demonstrates the formation of RIPs as a result of charge separation. The T_1 state at these early times ($t < 1$ ns) is not populated, since all RIPs are born in the singlet state.

Further evolution of singlet RIPs is determined primarily by competition between (a) the diffusive decay of the geminate RIPs with release of the free ions into the bulk, (b) back electron transfer to the ground state S_0 (singlet charge recombination) and (c) their transformation into the triplet RIPs as a result of HFI and/or interaction with an external magnetic field via the Δg-mechanism. It should be noted here that charge recombination of singlet RIPs in DMeA/PN is rather slow due to large energy gap between the *CSS* and S_0 energy levels ($\Delta G_{CR0} = -2.58$ eV), that puts the CR0 reaction into the Marcus inverted region. However, the CR0 channel remains to be dominant for the RIP decay up to 5 ns, since the geminate ions at these early stages are still at the close-to-contact distances and the HFI intensity is not enough to flip the electron spins and transform the singlet RIP into the triplet one.

Table 1 Values of model parameters used in simulations (prototype system: DMeA/PN in ACN solution [21])

No	Parameter description	Notation	Value
1	F^* fluorescence lifetime (without quenchers)	τ_F	7.9 ns
2	Concentration of quenchers	c	0.4 M
3	Contact radius of reactants	σ	6 Å
4	Static dielectric constant of solvent	ϵ_0	36
5	Optical dielectric constant of solvent	ϵ_∞	1.8
6	Longitudinal solvent relaxation time	τ_L	0.5 ps
7	Encounter diffusion coefficient	D	370 $Å^2$/ns
8	Bath temperature	$k_B T$	0.025 eV
9	Free energy of solvent reorganization at $r = \sigma$	λ_m	0.75 eV
10	Low-frequency intramolecular reorganization energy	λ_i	0.0
11	High-frequency intramolecular reorganization energy	λ_q	0.342 eV
12	S_0 energy level	E_{S0}	0.0
13	S_1 energy level	E_{S1}	3.08 eV
14	T_1 energy level	E_{S0}	1.67 eV
15	*CSS* energy level at $r = \sigma$	E_{CSS}	2.58 eV
16	Solvent polarization fluctuation length	Λ	1.6 Å
17	Electron tunnelling length	L	1.0 Å
18	CT coupling energies for CS, CR0 and CR1 at $r = \sigma$	V_0	0.021 eV
19	Frequency of the effective intramolecular quantum mode	$\hbar\Omega$	0.15 eV
20	Electron-vibrational couplings for CS, CR0 and CR1	S	2.28
21	Isotropic hyperfine interaction constant	A	0.4 ns^{-1}
22	Exchange interaction in radical-ion pairs	J	0

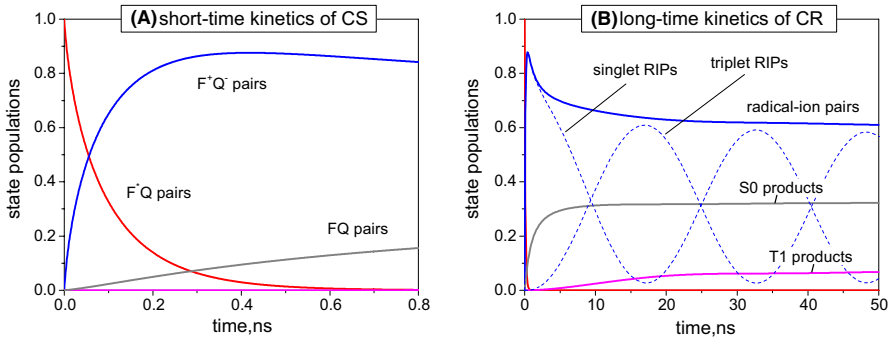

Fig. 3 **A** Simulated kinetics of the excited state S_1 (red), charge-separated state *CSS* (blue), ground state S_0 (grey), and triplet excited state T_1 (magenta) in the [0, 0.8] ns time interval. Fast decay of the F^*Q pairs with simultaneous raise of the F^+Q^- pair population indicates efficient quenching of F^* fluorescence by electron transfer to Q. **B** The same kinetics as A, but over a longer time interval [0, 50] ns. Slow decay of the RIP population (blue curve) is a result of charge recombination of the singlet and triplet RIPs to the S_0 and T_1 states, respectively. The HFI-induced coherent spin dynamics are illustrated by time-dependent populations of the singlet and triplet RIPs (dashed blue lines). Here $\omega_D = \omega_A = 0$ (zero field), $A = 0.4\ ns^{-1}$, other parameters are listed in Table 1 (Color figure online)

The role of the HFI-induced spin transitions in these processes becomes more prominent at somewhat longer time scales, as illustrated in Fig. 3B, where the *CSS*, S_0 and T_1 populations are displayed up to 50 ns. The total RIP population (solid blue line) is shown here together with two its individual components—the singlet and triplet subpopulations (dashed lines). Coherent spin evolution apparently leads to the delayed recombination of triplet RIPs and the T_1 product formation (magenta line). It is also seen in Fig. 3B that at $t = 50$ ns the geminate processes are mostly over, the ions have already left the recombination layer and escaped to the bulk.

It is clear that the relationship between the singlet and triplet products of charge recombination is determined not only by details of spin conversion in RIPs, but the diffusive motion of ions as well. Particularly interesting in this case may be the situation when the RIP formation and the RIP decay processes (due to CS and CR, respectively) proceed at different inter-particle distances. In this case, the newly born F^+ and Q^- ions must first reach the CR reaction layer before they can recombine, and their spin state can change during this time interval. Similar effects can be observed if there is a significant shift between the singlet and triplet CR layers. In this case one can expect both spin- and distance-dependent recombination of ions, where the reactant's diffusion plays an important role.

It should be noted that the arrangement of the DMeA/PN energy levels actually facilitates the aforementioned shift between the CR0 and CR1 recombination layers. Indeed, the recombination of singlet RIPs in this system is highly exergonic ($\Delta G_{CR0} = -2.58$ eV) and proceeds in the Marcus inverted region, while the CR1 exergonicity is much lower ($\Delta G_{CR1} = -0.91$ eV) and corresponds to a low-barrier or even barrierless reaction. Taking into account the r-dependence of the $W_{RT}(r)$ and $W_{RS}(r)$ coupling functions from Eq. 17, one can expect the triplet RIPs to recombine primarily at contact distances, while the singlet recombination to proceed in more "loose" ion pairs.

To estimate the arrangement of the CS, CR0 and CR1 reaction layers in the DMeA/PN system we calculated the r-distributions of the reactants and products of these processes. In Fig. 4A, the density of the F*Q pairs (the $n(r, t)$ function

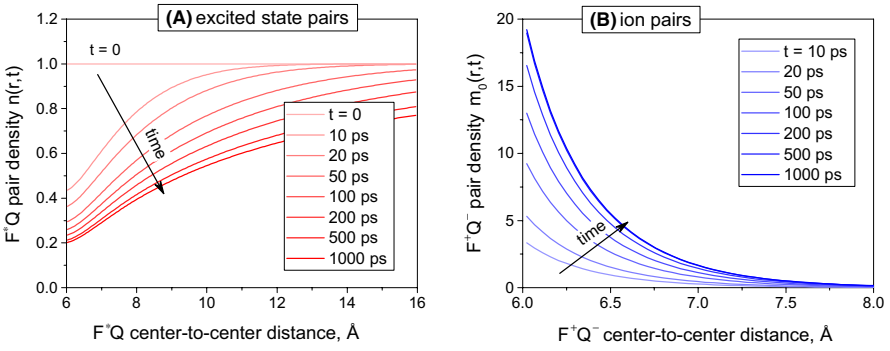

Fig. 4 **A** Distribution of the excited fluorophore–quencher pairs over the distances r between the partners at different instants of time t. **B** Spatial distribution of RIPs formed in the CS reaction. The values of the model parameters are the same as in Fig. 3

introduced previously) is shown as a function of r at different t's. This graph shows fast depletion of $n(r, t)$ around the contact ($r = \sigma = 6$ Å) at very short-time scales $t < 10 - 50$ ps. This phenomenon is often referred to as the static quenching [26], since at these early stages the reactants are almost immobile, and the electron transfer from F^* to Q proceeds primarily in tight F^*Q pairs. The ion pairs formed in the course of this initial static quenching have similar spatial distribution in vicinity of $r = \sigma$, as illustrated in Fig. 4B.

At the same time, the *CSS* population decay due to back electron transfer from Q^- to F^+ is strongly affected by the spin state of the RIP, as demonstrated by simulation results in Fig. 5. The figure shows the normalized r-distributions of the singlet and triplet ion pairs immediately before their recombination. Although the maximum of the singlet RIP density function is still at $r = \sigma$, there are significant differences between the spatial distributions of the recombined singlet and triplet RIPs here. As it was mentioned above the physical reason of this phenomenon is strong exergonicity of the CR0 reactions, which promotes electron tunnelling between the remotely located ions in the Marcus inverted region [26, 42].

One of manifestations of coherent spin transitions in radical pairs may be an oscillating kinetics of the CR product state. In the model considered, the oscillating T_1 population can serve as an indicator of a synchronized evolution of the electron spins and thus periodic modulation of the $CR1$ rate. To illustrate this point we consider the T_1 accumulation kinetics in the CS/CR reactions assisted by HFI. Figure 6A shows the simulated $P_{T1}(t)$ dependencies for the case $B = 0$ (no external magnetic field, solid blue curve) and $B = 150$ mT (strong saturating magnetic field, dashed blue curve), that demonstrate the pronounced oscillatory components. To quantify the influence of a strong magnetic field on $P_{T1}(t)$ in these reactions we define the time-dependent magnetic field effect (MFE) as follows:

$$\chi(t) = \frac{P_{T1}^{(B=0)}(t) - P_{T1}^{(B=150)}(t)}{P_{T1}^{(B=0)}(t)}. \tag{19}$$

This quantity is shown in Fig. 6B.

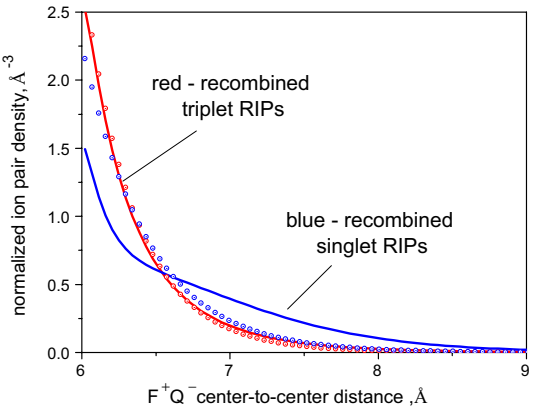

Fig. 5 Normalized distributions of the triplet (blue line) and singlet (red line) RIPs immediately before their recombination to T_1 and S_0, respectively. These curves demonstrate the shift between the singlet and triplet recombination layers, which also affects the distribution of inter-particle distances in the CR0 and CR1 products. Red and blue dots indicate the normalized $W_{CS}(r)$ and $W_{CR}(r) = W_{RS}(r) + W_{RT}(r)$ dependencies for comparison (Color figure online)

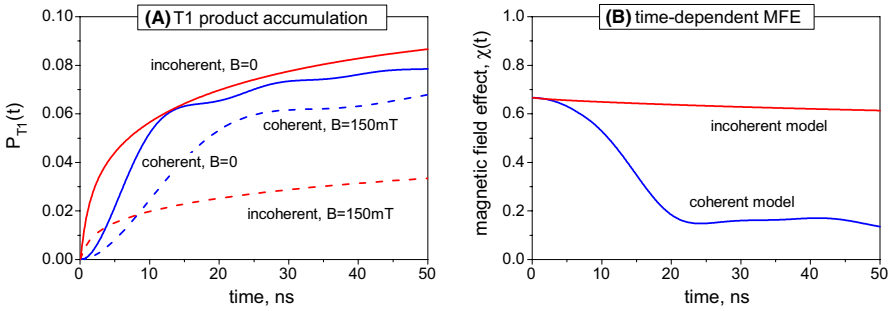

Fig. 6 **A** T_1 population kinetics simulated in zero (solid lines) and saturated magnetic fields (dashed lines). The results of the coherent and incoherent (kinetic) models of singlet–triplet conversion are shown in blue and red, respectively. **B** Time-dependent magnetic field effect $\chi(t)$ (see Eq. (19)) in the case of coherent HFI-induced spin transitions (blue) and within the $k_S/3k_S$ rate description (red) (Color figure online)

Consider now the well-known simplistic model of spin conversion, in which the singlet–triplet (ST) and the triplet–singlet (TS) transitions are treated as the kinetic (first-order) processes and described phenomenologically with the rate constants k_{ST} and k_{TS} [26, 42]. In the zero field limit ($B = 0$), the four spin states of the RIP (S, T_0, T_+ and T_-) are assumed to be degenerate, so that hyperfine interactions can effectively mix their populations. To ensure proper equilibration of all populations at $t \to \infty$ with the final singlet and triplet values $P_S = 0.25$ and $P_T = P_{T_0} + P_{T_+} + P_{T_-} = 0.75$, the rate of the ST-transitions is commonly taken to be 3 times larger than the rate of the TS-transitions, $k_{ST} = 3k_{TS} = 3k_S$. The k_S quantity here is a phenomenological parameter of the model.

This kinetic model has been repeatedly used for the analysis of the zero-field spin effects in radical reactions [26, 42]. It was shown in Ref. [17], that in the case of fast triplet recombination, the $k_S/3k_S$-model gives exactly the same asymptotic values of the T_1 product yield as the coherent model with isotropic HFI provided that k_S and A are related as

$$k_S = \frac{A}{32}. \tag{20}$$

To approve the applicability of the simplified kinetic approach to reactions under consideration, we apply it to the theory presented above and replace the Hamiltonian dynamics of $\hat{m}(r,t)$ in Eq. (9) by a set of the two coupled diffusion–reaction equations for the singlet and triplet RIP densities

$$\begin{aligned}
\frac{\partial m_S(r,t)}{\partial t} &= \hat{L}m_S(r,t) - 3k_S m_S(r,t) + k_S m_T(r,t) - W_{RS}(r)m_S(r,t) + f_S(r,t),\\
\frac{\partial m_T(r,t)}{\partial t} &= \hat{L}m_T(r,t) - k_S m_T(r,t) + 3k_S m_S(r,t) - W_{RT}(r)m_T(r,t).
\end{aligned} \tag{21}$$

Here, $m_S(r,t) = m_{SS}(r,t)$ and $m_T(r,t) = m_{T_0T_0}(r,t) + m_{T_+T_+}(r,t) + m_{T\_T\_}(r,t)$ are the diagonal elements of the $\hat{m}(r,t)$ matrix. Using the relation (20) between k_S and A, and employing Eqs. (21) instead of Eq. (9), one obtains a kinetic analog for the theory presented above. The time-dependent populations of the singlet and triplet CR products then can be calculated as follows:

$$P_S(t) = c \int W_{RS}(r)\, m_S(r,t)\, d^3r,$$
$$P_T(t) = c \int W_{RT}(r)\, m_T(r,t)\, d^3r. \tag{22}$$

Figure6B shows that the rate model predicts weak time dependence of the magnetic field effect, while the coherent model demonstrates strong decrease in the effect over time. The initial values of the effect in both cases are 2/3. This is a direct consequence of the ratio of the populations of triplet ion pairs in zero and saturated magnetic fields, which for short times is 3:1 for both models [19]. This ratio remains practically unchanged over time for the rate model. Coherent spin conversion, on the other hand, predicts a significant decrease in this ratio with time [19], which leads to a strong decrease in the magnetic field effect.

It is instructive to compare the predictions of the two theories by analysing the numerical results shown in Fig. 6A. The $P_{T1}(t)$ kinetics presented here are calculated within the coherent ($A = 0.4$ ns^{-1}, solid blue line) and incoherent ($k_S = A/32$, solid red line) models of spin conversion in zero magnetic field. It should be noted that despite of the visible differences between the blue and red curves up to $t = 50$ ns, both models give rather close $P_{T1}(t)$ values at longer time intervals (not shown in the figure). This confirms the correctness of the analysis presented in Ref. [17]. On the contrary, the early time $P_{T1}(t)$ kinetics in Fig.6A demonstrate essential distinctions between the Hamiltonian and kinetic descriptions of the spin subsystem. Indeed, the initial rise of the T_1 population in the [0, 5 ns] interval is clearly quadratic in time ($\propto t^2$) for the blue curve, while the red one is linear in t. This result reflects the well-known property of inertness of quantum systems, and also shows the limited applicability of kinetic models for describing spin dynamics at short times. It should be noted that experimental data indicate quadratic $P_{T1}(t)$ dependencies supporting the coherent mechanism of spin conversion in the DMeA/PN pair [21].

In fact, the $k_S/3k_S$-model itself has much wider region of applicability than Eq. (20), which is correct only for the HFI-induced spin transitions in zero magnetic field if the following conditions are fulfilled [17]

$$\eta_T \gg \eta_S, \theta, 1. \tag{23}$$

Here $\theta = \sqrt{A\sigma^2/2D}$, $\eta_S = k_c^{CR0}/k_D$, $\eta_T = k_c^{CR1}/k_D$, where $k_D = 4\pi\sigma D$ and k_c^{CR0}, k_c^{CR1} are calculated as

$$k_c^{CR0} = \int W_{RS}(r)\, d^3r, \qquad k_c^{CR1} = \int W_{RT}(r)\, d^3r. \tag{24}$$

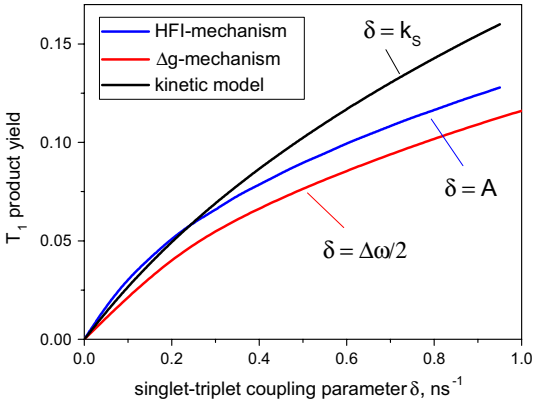

Fig. 7 T_1 product yield (Y_{T1}) as a function of the RIP singlet–triplet coupling parameter δ. The three curves correspond to the three different mechanisms of ST conversion as indicated in the figure. The corresponding coupling parameters are: $\delta = A$ for HFI (blue), $\delta = \Delta\omega$ for Δg interactions with magnetic field (red), and $\delta = k_S$ for the kinetic model in zero field (black) (Color figure online)

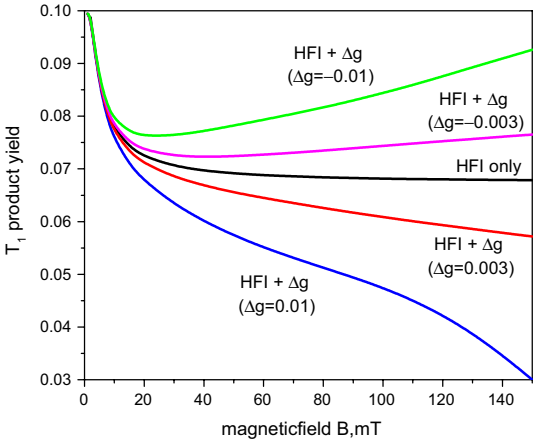

Fig. 8 T_1 product yield as a function of the magnetic field B in the model with two mechanisms of spin conversion in RIPs. The HFI constant is $A = 0.4\ \text{ns}^{-1}$, the values of the Δg parameter are indicated in the figure. Other parameters are listed in Table 1

Using Eqs. (17) and known parameters of the model, one can easily obtain the following estimates for the kinetic CR rates: $k_c^{CR0} = 0.47\ \text{Å}^2/\text{ps}$ and $k_c^{CR1} = 1168\ \text{Å}^2/\text{ps}$. These values allow us to calculate the dimensionless quantities: $\eta_T = 41.9$, $\eta_S = 0.017$, $\theta = 0.139$. The applicability conditions (23) are thus satisfied in DMeA/PN.

The influence of the ST-conversion mechanism on the T_1 product yield at the geminate stage is illustrated in Fig. 7. Despite the fact that the dynamics of ST transitions differs greatly over short times, it can be seen that for $k_S = A/32$ and $\Delta\omega = A/2$, all mechanisms predict quite similar results for the triplet state quantum yield.

The dependence of the quantum yield of the neutral triplet products on the magnetic field strength is pictured in Fig. 8. The addition of the Δg-mechanism can result in both an enhancement and an attenuation of MFE relatively to the HFI mechanism only. When the quantities A and $\Delta\omega$ are of the same sign, the two mechanisms enhance each other, since they function mainly in phase. In this case, a

strong suppression of the triplet product's yield is possible in an external magnetic field (blue and red lines in Fig. 8). When the signs of A and $\Delta\omega$ are the opposite, the two mechanisms act in anti-phase that attenuates the magnetic field effect (magenta and green lines in Fig. 8). The saturation of the magnetic field effect on the triplet product yield, which is well known for the HFI mechanism, disappears in RIPs with $\Delta g > 0.001$ in moderate magnetic fields $B < 150$ mT.

4 Conclusions

The kinetics of radical ion pair formation by photoinduced electron transfer in solutions, as well as the kinetics of the population of triplet products of their recombination, has been simulated. In the case of HFI-induced spin transitions, the time-dependent magnetic field effect on the triplet product population of the RIPs recombination is explored. This effect is large in early times and decreases greatly with time. When the spin evolution of singlet born RIPs is induced by both the HFI and Δg mechanisms, their mutual action can result in both an enhancement and an attenuation of the magnetic field effect relatively to a single HFI mechanism. The enhancement of the magnetic field effect can lead to complete suppression of the neutral triplet product formation.

The effect of suppressing the yield of triplet neutral products in moderate magnetic fields can be used to increase the effectiveness of emerging photovoltaic organic devices. The things are, in real RIPs, the charge recombination of triplet pairs often occurs much faster than that of singlet pairs, due to the more favorable free energy gap. As a result, singlet–triplet transitions in RIPs can greatly accelerate charge recombination of the singlet-born RIPs. Indeed, it has been shown that singlet–triplet transitions in RIPs significantly reduce the efficiency of photovoltaic organic devices due to the acceleration of charge recombination [43–45]. In such devices, charge recombination is an undesirable process leading to a decrease in their efficiency; therefore, mechanisms for suppressing charge recombination with the formation of triplet products are in great demand.

Funding The work is supported by the Russian Foundation for Basic Research (project No. 19-03-00175).

References

1. K.M. Salikhov, Y.N. Molin, R.Z. Sagdeev, A.L. Buchachenko, *Spin Polarization and Magnetic Effects in Radical Reactions Akademian Kiado (Budapest)* (Elsevier, Amsterdam, 1984)
2. A. Weller, Pure Appl. Chem. **54**, 1885 (1982). https://doi.org/10.1351/pac198254101885
3. I.R. Gould, S. Farid, Acc. Chem. Res **29**, 522 (1996). https://doi.org/10.1021/ar950053z
4. N. Mataga, H. Miyasaka, Adv. Chem. Phys. **107**, 431 (1999). https://doi.org/10.1002/9780470141663.ch8
5. A. Rosspeintner, E. Vauthey, Phys. Chem. Chem. Phys. **16**, 25741 (2014). https://doi.org/10.1039/C4CP03862B

6. K. Schulten, H. Staekand, A. Weller, H.J. Werner, B.Z. Nickel, Z. Phys. Chem. **101**, 371 (1976). https://doi.org/10.1524/zpch.1976.101.1-6.371
7. Z. Schulten, K. Schulten, J. Chem. Phys. **66**, 4616 (1977). https://doi.org/10.1063/1.433719
8. A. Weller, H. Staerk, R. Treichel, Faraday Discuss. Chem. Soc. **78**, 271 (1984). https://doi.org/10.1039/DC9847800271
9. M. Ottolenghi, Acc. Chem. Res. **6**, 153 (1973). https://doi.org/10.1021/ar50065a002
10. M.E. Michel-Beyerle, R. Haberkorn, W. Bube, E. Steffens, H. Schroeder, H.J. Neusser, E.W. Schlag, H. Seidlitz, Chem. Phys. **17**, 139 (1976). https://doi.org/10.1016/0301-0104(76)80097-3
11. B. Brocklehurst, J. Chem. Soc. Faraday Trans. **72**, 1869 (1976). https://doi.org/10.1039/F29767201869
12. H.J. Werner, H. Staerk, A. Weller, J. Chem. Phys. **68**, 2419 (1978). https://doi.org/10.1063/1.436013
13. A.A. Neufeld, A.I. Burshtein, G. Angulo, G. Grampp, J. Chem. Phys. **116**, 2472 (2002). https://doi.org/10.1063/1.1433746
14. G. Angulo, G. Grampp, A.A. Neufeld, A.I. Burshtein, J. Phys. Chem. A **107**, 6913 (2003). https://doi.org/10.1021/jp0342475
15. V.S. Gladkikh, A.I. Burshtein, G. Angulo, G. Grampp, Phys. Chem. Chem. Phys. **5**, 2581 (2003). https://doi.org/10.1039/B301009K
16. K.M. Salikhov, Chem. Phys. **82**, 145 (1983). https://doi.org/10.1016/0301-0104(83)85353-1
17. D.V. Dodin, A.I. Ivanov, A.I. Burshtein, J. Phys. Chem. A **112**, 889 (2008). https://doi.org/10.1021/jp077725a
18. A.I. Ivanov, A.I. Burshtein, J. Phys. Chem. A **112**, 6392 (2008). https://doi.org/10.1021/jp800008n
19. D.V. Dodin, A.I. Ivanov, A.I. Burshtein, J. Chem. Phys. **138**, 124102 (2013). https://doi.org/10.1063/1.4795576
20. A.I. Burshtein, A.I. Ivanov, J. Chem. Phys. **141**(2), 024508 (2014)
21. S.V. Feskov, M.V. Rogozina, A.I. Ivanov, A. Aster, M. Koch, E. Vauthey, J. Chem. Phys. **150**(2), 024501 (2019)
22. K. Möbius, W. Lubitz, A. Savitsky, Appl. Magn. Reson. **41**(2), 113 (2011). https://doi.org/10.1007/s00723-011-0284-7
23. U.E. Steiner, T. Ulrich, Chem. Rev. **89**, 51 (1989). https://doi.org/10.1021/cr00091a003
24. A.I. Burshtein, Chem. Phys. Lett. **194**, 247 (1992). https://doi.org/10.1016/0009-2614(92)85542-I
25. R.C. Dorfman, M.D. Fayer, J. Chem. Phys. **96**, 7410 (1992). https://doi.org/10.1063/1.462391
26. A.I. Burshtein, Adv. Chem. Phys. **114**, 419 (2000). https://doi.org/10.1002/9780470141731.ch6
27. A. Rosspeintner, D.R. Kattnig, G. Angulo, S. Landgraf, G. Grampp, A. Cuetos, Chem. Eur. J. **13**(22), 6474 (2007). https://doi.org/10.1002/chem.200700106
28. S.V. Feskov, A.I. Burshtein, J. Phys. Chem. A **113**(48), 13528 (2009). https://doi.org/10.1021/jp901863t
29. G. Angulo, A. Rosspeintner, B. Lang, E. Vauthey, Phys. Chem. Chem. Phys. **20**(39), 25531 (2018). https://doi.org/10.1039/C8CP05153D
30. A. Reymond, G.K. Fraenkel, J. Phys. Chem. **71**, 4570 (1967). https://doi.org/10.1021/j100872a076
31. I.C. Lewis, L.S. Singer, J. Chem. Phys. **43**, 2712 (1965). https://doi.org/10.1063/1.1697200
32. N.N. Lukzen, J.B. Pedersen, A.I. Burshtein, J. Phys. Chem. A **109**, 11914 (2005). https://doi.org/10.1021/jp053539y
33. N. Korst, A. Lazarev, Physica **42**(1), 31 (1969). https://doi.org/10.1016/0031-8914(69)90085-8
34. J.B. Pedersen, J.H. Freed, J. Chem. Phys. **58**(7), 2746 (1973). https://doi.org/10.1063/1.1679576
35. J.B. Pedersen, J.H. Freed, J. Chem. Phys. **59**(6), 2869 (1973). https://doi.org/10.1063/1.1680418
36. A.A. Kornyshev, J. Ulstrup, Chem. Phys. Lett. **126**, 74 (1986). https://doi.org/10.1016/0009-2614(86)85119-3
37. R.A. Marcus, N. Sutin, Biochim. Biophys. Acta **811**, 265 (1985). https://doi.org/10.1016/0304-4173(85)90014-X
38. K. Huang, A. Rhys, Proc. R. Soc. A **204**, 406 (1950). https://doi.org/10.1098/rspa.1950.0184
39. S.V. Feskov, Math. Phys. Comput. Simul. **24**(1), 50 (2021). https://doi.org/10.15688/mpcm.jvolsu.2021.1.4
40. M. Koch, G. Licari, E. Vauthey, J. Phys. Chem. B **119**, 11846 (2015). https://doi.org/10.1021/acs.jpcb.5b07663

41. E. Pines, D. Huppert, N. Agmon, J. Chem. Phys. **88**, 5620 (1988). https://doi.org/10.1063/1.454572
42. A.I. Burshtein, Adv. Chem. Phys. **129**, 105 (2004). https://doi.org/10.1002/047168077X.ch3
43. F. Etzold, I. Howard, N. Forler, A. Melnyk, D. Andrienko, M. Hansen, F. Laquai, Energy Environ. Sci. **8**, 1511 (2015). https://doi.org/10.1039/C4EE03630A
44. R.M. Williams, H.C. Chen, D.D. Nuzzo, S.C.J. Meskers, R.A.J. Janssen, J. Spectrosc. **2017**, 1 (2017). https://doi.org/10.1155/2017/6867507
45. E.M. Espinoza, D. Bao, M. Krzeszewski, D.T. Gryko, V.I. Vullev, Int. J. Chem. Kinet. **51**(9), 657 (2019). https://doi.org/10.1002/kin.21285